

## Efficacy of the Method of Four Coefficients to Determine Charge-Carrier Scattering

Caitlin M. Crawford<sup>1,\*</sup>, Erik A. Bensen<sup>1</sup>, Haley A. Vinton<sup>2</sup>, and Eric S. Toberer<sup>1,3</sup>

<sup>1</sup>*Physics Department, Colorado School of Mines, Golden, Colorado 80401, USA*

<sup>2</sup>*Mathematics Department, Colorado School of Mines, Golden, Colorado 80401, USA*

<sup>3</sup>*National Renewable Energy Laboratory, Golden, Colorado 80401, USA*

 (Received 17 November 2020; revised 3 April 2021; accepted 28 June 2021; published 3 August 2021)

The investigation of the electronic properties of semiconductors from transport measurements (i.e., resistivity, Hall, and Seebeck coefficient measurements) is challenging due to the averaging of charge-carrier dynamics inherent in such measurements. Here, we investigate the incorporation of a fourth measurement of electronic transport, the Nernst coefficient, into the analysis, termed the method of four coefficients. This approach yields the Fermi level, effective mass, scattering exponent, and relaxation time prefactor. We begin with a review of the underlying mathematics and investigate the mapping between the four-dimensional material property and transport coefficient spaces. We then investigate how the traditional single-parabolic band method yields a single, potentially incorrect point on the solution subspace. This uncertainty can be resolved through Nernst coefficient measurements and we map the span of the ensuing subspace. We conclude with an investigation of how sensitive the analysis of transport coefficients is to experimental error for different sample types.

DOI: [10.1103/PhysRevApplied.16.024004](https://doi.org/10.1103/PhysRevApplied.16.024004)

### I. INTRODUCTION

Holistic design strategies for novel semiconductors require an understanding on how charge-carrier scattering is driven by chemical composition and microstructure [1,2]. The challenge to date is the difficulty in resolving scattering sources and strengths as a function of charge-carrier energy. Historically, most analyses prescribe a value to the energy dependence of scattering and simply incorporate scattering into a mobility value [3,4]. Galvanothermometric measurements, such as Nernst, can shed light on scattering if combined with other thermoelectric characterization techniques [5,6]. However, this approach is nontrivial and few groups have a history of such multiparameter analysis [7–11]. In this work, we provide a comprehensive study of this transformation between experimental measurables and underlying material properties. We focus on case examples from thermoelectric materials, but the results are generalizable to other classes of semiconductors.

Majority charge-carrier transport is often characterized via three effects: electrical conductivity, Hall effect, and the Seebeck effect. Together these three coefficients are frequently used in conjunction to make inferences about the underlying transport phenomena [12]. In the field of thermoelectrics, it is common practice to assume

an electronic band structure (e.g., parabolic) and scattering type to approximate an effective mass ( $m^*$ ), reduced Fermi level ( $\eta = E_F/k_B T$ , where  $E_F$  is the Fermi level), and Hall mobility ( $\mu_H$ ) for a system. The combination of the three transport coefficients is colloquially known as the single-parabolic band (SPB) model; see Fig. 1 [13–15]. This three-coefficient approach is favored for its simplicity and accessibility through common thermoelectric measurement techniques. This approach is often appropriate when a dominant scattering mechanism can be inferred from temperature-dependent measurements. Furthermore, the common use of this analysis technique has facilitated comparisons between research groups [2].

Despite these attractive features, the SPB model has significant pitfalls when analyzing chemical trends. Specifically, changes in carrier transport are often attributed to changes in effective mass or mobility. However, a change in the dominant scattering mechanism of the system could result in similar alterations in materials properties [16]. This is particularly pernicious in chemical systems containing aliovalent alloys and deleterious dopants. As such, an approach to investigate the dominant scattering mechanism is needed.

In order to eliminate the assumption of a particular dominant scattering mechanism, a fourth measurable must be introduced to solve for our four unknown material parameters: reduced Fermi level, scattering

\*caitlincrawford@mines.edu

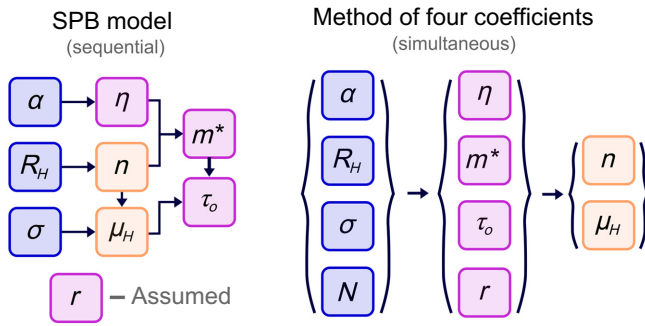


FIG. 1. The SPB model begins by assuming a scattering exponent ( $r$ ) that correlates to a dominate scattering mechanism. Sequential analysis of transport coefficients (blue) then yields the fundamental material parameters (pink) of interest. In order to eliminate this scattering assumption and thus determine more accurate underlying material properties, a fourth coefficient (Nernst,  $N$ ) can be included. As such, the method of four coefficients can be used to accurately probe scattering sources in semiconductors.

time prefactor, effective mass, and scattering exponent ( $\eta$ ,  $\tau_0$ ,  $m^*$ ,  $r$ , respectively). The method of four coefficients introduces a fourth transport coefficient to eliminate the assumption of scattering exponent. This approach manipulates the Seebeck effect, electrical conductivity, the Hall effect, and the transverse Nernst effect as seen in Fig. 1 [17]. An uncommon thermoelectric measurement, the Nernst effect produces a measurable transverse voltage when a longitudinal temperature gradient and out-of-plane magnetic field are applied [18,19]. The sign of the Nernst coefficient depends on the scattering parameter of the system and the band structure [20]. By adding this fourth coefficient to the analysis, the assumption of scattering type can be eliminated and therefore investigated. As such, the method of four coefficients allows us to resolve the reduced Fermi level ( $\eta$ ), density of states effective mass ( $m^*$ ), constant relaxation time ( $\tau_0$ ), and scattering exponent ( $r$ ) from four experimentally measured values.

In 1966, Zhitinskaya *et al.* [17] introduced the concept of *the method of four coefficients* to investigate the scattering effects on the nonparabolicity of the band structure in PbTe. However, this approach has been historically underutilized. Before 2000, most research was focused on the measurement techniques and the theory behind the method [11,21–27]. Starting in the 2000s, several research groups began utilizing the method of four coefficients to perform analysis on experimental data [28,29].

For example, in 2008, Jovic *et al.* [30] used the method of four coefficients to investigate Fermi level pinning at low temperature in indium doped Pb-Sn-Te alloys. Ultimately, it was concluded that changes in transport were not linked to indium doping as evidenced by the lack of deviation expected in effective mass, which was

analyzed via the method of four coefficients. Similar strategies to understand trends in chemical modification via this method have been used to investigate the presence of resonant energy states as evidenced by abnormal changes in effective mass [10,16,31].

Outside of thermoelectric materials, the method of four coefficients has been applied to thin-film transparent conducting oxide materials for photovoltaic applications. These works focused on determining which underlying material parameter limits majority carrier mobility, one of the key material parameters in transparent conductors [7,29,32,33].

The efforts discussed above connect the measured scattering exponent,  $r$ , to specific scattering mechanisms (e.g., acoustic phonons, ionized defects). In reverse, experimental estimations of  $r$  are increasingly vital for assessing the accuracy of first-principles scattering calculations. The last decade has seen significant advances in estimating electron-phonon scattering rates from first-principle calculations [34–39]. While these calculations help understand the core electronic transport of a material, they lack experimental validation. For systems with multiple scattering sources, Matthiessen’s rule leads to predictions of the overall scattering exponent that is often quite different than the classic analytic expressions. Consequently, the method of four coefficients could be used to help aid in the verification of these calculations due to its ability to determine a real-valued scattering exponent near the Fermi level.

In this paper we focus on the method of four coefficients and its effects on thermoelectric measurements. Using a SPB assumption, we perform analysis on the four-dimensional space and determine regions of potentially large Nernst effect signal. We consider how the SPB method, with three coefficients, could lead to erroneous conclusions concerning the underlying material parameters. In addition, we address how uncertainty in experimental measurements will affect the results of this approach.

## II. TRADITIONAL SINGLE-PARABOLIC BAND ANALYSIS

The thermoelectrics community has historically focused on a three-coefficient isotropic single-parabolic band analysis, commonly referred to as the SPB model. Here experimental measurements of the Seebeck effect, the Hall effect, and conductivity are used to determine Fermi level ( $E_F$ ), density of states effective mass ( $m^*$ ), and Hall mobility ( $\mu_H$ ) [12]. In order to decouple these material parameters from the measured coefficients, it is common to make various assumptions to simplify the analytics. It is assumed that power-law scattering is applicable and takes the form

$$\tau = \tau_0 \chi^{r-1/2}, \quad (1)$$

where  $\tau_0$  is the relaxation time prefactor and  $r$  is the energy-dependant exponent that is often correlated to a

dominate scattering mechanism of the system [3]. Here  $\chi$  is the reduced energy,  $\chi = E/k_B T$ , where  $k_B$  is Boltzmann's constant and  $T$  is the temperature. The scattering exponent (or parameter)  $r$ , as it is commonly called, has been calculated via Fermi's golden rule for common scattering types. Here  $r = 0$  for acoustic-phonon scattering,  $r = 2$  for ionized impurity scattering, and  $r = 1$  for polar optical phonons at high temperatures [40].

### A. Governing equations

We can construct equations for the three coefficients (Hall, conductivity, and Seebeck) in terms of the material parameters of interest ( $\eta$ ,  $m^*$ ,  $\tau_0$ , and  $r$ ) assuming an infinitely large band gap, parabolic band edge, and one carrier type [40]. The investigation of multiple samples at different carrier concentrations and temperatures is one strategy to ensure that these approximations hold. Gaussian units are used in this section and conversion factors to more traditional units can be found in Table 4 within the Supplemental Material [41]. With the approximation of an isotropic band, the electrical conductivity ( $\sigma$ ) can be expressed in terms of an energy-dependent integral

$$\sigma = ne\mu = ne^2 \left\langle \frac{\tau(E)}{m(E)} \right\rangle, \quad (2)$$

$$\text{where } \langle A \rangle = \frac{1}{3\pi^2 n} \int_0^\infty \left( -\frac{\partial f_0}{\partial E} \right) k^3(E) A(E) dE$$

with  $\partial f_0/\partial E$  the derivative of the Fermi-Dirac distribution with respect to energy and  $k$  the electron wavevector. The sign of the electric charge ( $e$ ) is dictated by the carrier type ( $e = -e$  for electrons and  $e = +e$  for holes). Also,  $A$  is a place-holder variable representing a general function and the  $\langle \rangle$  brackets are a short hand for the integral above. By substitution of the power-law scattering equation [Eq. (1)],  $\tau_0$  is pulled out of the integral and we are left with the energy-dependent term. Likewise, if we assume a single-parabolic band [ $k(E) = (2m^*E/\hbar^2)^{1/2}$ ], the effective mass is not dependent on energy, thereby allowing us to pull ( $1/m^*$ ) out front. Together, this gives us the equation

$$\begin{aligned} \sigma &= ne^2 \frac{\tau_0}{m^*} \langle \chi^{r-1/2} \rangle \\ &= \frac{e^2}{3\pi^2} \frac{\tau_0}{m^*} \int_0^\infty \left( -\frac{\partial f_0}{\partial \chi} \right) k^3 \chi^{r-1/2} d\chi. \end{aligned} \quad (3)$$

The integral of the energy-dependent terms can be rewritten as a one-parameter Fermi integral,  $F_r$ , of the form

$$F_r(\eta) = \int_0^\infty \left( -\frac{\partial f}{\partial \chi} \right) \chi^r d\chi, \quad (4)$$

where  $\chi$  is the reduced energy:  $\chi = E/k_B T$ . Inserting  $k(E)$  and simplifying the integral, the conductivity equation in

Eq. (3) can be rewritten as

$$\sigma = \frac{e^2 (2k_B T)^{3/2}}{3\pi^2 \hbar^3} m^{*1/2} \tau_0 F_{r+1}(\eta), \quad (5)$$

where  $\sigma$  depends on all four material parameters ( $\eta$ ,  $r$ ,  $m^*$ ,  $\tau_0$ ). Similar expressions can be obtained for the Seebeck coefficient ( $\alpha$ ) and Hall coefficient ( $R_H$ ) using their energy-dependent forms [see Eqs. (1)–(7) within the Supplemental Material [41]]. In the case of  $\alpha$ , the magnitude depends strictly on  $\eta$  and  $r$  while being independent of  $\tau_0$  and  $m^*$ :

$$\alpha = -\frac{k_B}{e} \left( \frac{F_{r+2}(\eta)}{F_{r+1}(\eta)} - \eta \right). \quad (6)$$

Similarly,  $R_H$  is independent of  $\tau_0$ :

$$R_H = -\frac{1}{ec} \left( \frac{F_{2r+1/2}(\eta)}{[F_{r+1}(\eta)]^2} \right) \left( \frac{3\pi^2 \hbar^3}{(2m^*k_B T)^{3/2}} \right). \quad (7)$$

To fit the convention of literature, the more intuitive unit of carrier concentration is used instead of the Hall coefficient. To convert between the two for the SPB model approach, the Hall equation is solved for in terms of carrier concentration while assuming the Hall factor is unity ( $a_r = 1$ ):

$$n = \frac{a_r}{R_H e c}, \quad a_r = \frac{F_{3/2}(\eta) F_{2r+1/2}(\eta)}{[F_{r+1}(\eta)]^2}. \quad (8)$$

For acoustic-phonon scattering,  $a_r = 1.18$ , and for neutral impurity scattering,  $a_r = 1.00$ . A more extensive list of Hall factors may be found in Table 6 within the Supplemental Material [41]. SPB analysis often assigns a Hall factor of unity even though this three-coefficient method often uses acoustic-phonon scattering ( $r = 0$ ) as the dominate scattering mechanism [42]. The standard order of operations for the SPB model can be seen in Fig. 1. This analysis begins by assuming that the dominate scattering mechanism is acoustic-phonon scattering and, as such,  $r = 0$  remains fixed throughout this approach. The first step begins by solving for  $\eta$  from the Seebeck coefficient via Eq. (6). Once  $\eta$  is determined, the effective mass can be solved for by using  $\eta$  and the carrier concentration. By combining Eqs. (7) and (8), an explicit form of carrier concentration can be derived:

$$\begin{aligned} n &= \frac{(2m^*k_B T)^{3/2}}{3\pi^2 \hbar^3} F_{3/2}(\eta) \rightarrow m^* \\ &= \left( \frac{n}{F_{3/2}(\eta)} \frac{3\pi^2 \hbar^3}{(2k_B T)^{3/2}} \right)^{2/3}. \end{aligned} \quad (9)$$

Finally, the mobility  $\mu$ , or, more often the Hall mobility  $\mu_H$ , can be extracted from these measurements. The Hall

mobility differs from  $\mu$  by the Hall factor  $a_r$ :  $\mu_H = a_r\mu$ , where  $a_r$  can be found in Eq. (8) [42]. The Hall factor within the SPB model is often assumed to be unity. When this approximation is made, the Hall mobility is simply calculated via the simple form of conductivity as seen in Eq. (2):  $\mu_H = \sigma/ne$  [43]. The reason we often focus on Hall mobility ( $\mu_H$ ) instead of the true mobility ( $\mu$ ) is that determining  $a_r$  requires knowledge of  $\eta$  and  $r$  [see Eq. (8)], which requires an additional transport measurement. Though not often reported, one could discern  $\tau_0$  via the mobility,  $\mu = \langle \tau(E)/m^* \rangle$ , as

$$\tau_0 = \mu \frac{m^* F_{3/2}(\eta)}{e F_{r+1}(\eta)}. \quad (10)$$

We emphasize that this equation is for  $\mu$  and not  $\mu_H$ .

As seen by Eqs. (5)–(7), these three transport measurements are linked to three underlying material properties ( $\eta$ ,  $m^*$ , and  $\tau_0$ ) (when assuming a scattering exponent). As such, one could determine expected values of transport coefficients for a wide range of material parameters. In Fig. 2(a), we construct a three-dimensional domain based on realistic ranges for such parameters:  $1 \times 10^{-15} \text{ s} \leq \tau_0 \leq 1 \times 10^{-14} \text{ s}$ ;  $0.1m_e \leq m^* \leq 3.5m_e$ ;  $-5 \leq \eta(E_F/k_B T) \leq 10$ . This domain space spans a wide region of semiconductors as evidenced by the large range of Fermi level positions well below and well above the band edge ( $\eta = 0$ ). As a reminder, we have assumed an infinitely large band gap and one carrier type; as a result, no bipolar conduction occurs.

In addition to the Fermi level range, high performing thermoelectric materials have been known to have high mobility values and thus large  $\tau_0$  and small  $m^*$  values. By including low values of  $\tau_0$  and high values of  $m^*$ , we can

also discern expected transport coefficients when mobility is limited. Again,  $r = 0$  is assumed here for the SPB model approach. Using the ranges determined in Fig. 2(a), we solve for the three electronic transport coefficients as seen in Fig. 2(b). Here, the more widely reported mobility value is heat mapped to the volume.

Using the domain ranges as described in Fig. 2(a), the calculated coefficients take on realistic ranges. The carrier concentration spans across roughly 6 orders of magnitude where higher values of carrier concentration display higher values in conductivity and lower values in the Seebeck coefficient, which is to be expected [orange point in Fig. 2(b)]. How the material parameters manifest themselves in the trend of these coefficients can be demonstrated by the mobility heat map on the coefficient volume. The high mobility region exists at the blue point in Fig. 2(b). This corresponds to the same blue point in Fig. 2(a) that has the expected high  $\tau_0$  and low  $m^*$  needed for high mobility. If we were to move across the domain space edge from the blue point to the green point in Fig. 2(a), we would be keeping our Fermi level and scattering time fixed but increasing the effective mass. How the coefficients trend from this vector can be seen in Fig. 2(b) by moving across the same direction (blue point  $\rightarrow$  green point). Unsurprisingly, the mobility decreases due to an increase in the effective mass. Other trends from the material parameters to the transport coefficient can be investigated through this lens.

As evident by the lack of deformation to this volume, this transformation has unique solutions. As such, the combination of three material parameters [blue point in Fig. 2(a)] correlates to one point in the coefficient space and vice versa [blue point in Fig. 2(b)]. Figures 2(a) and 2(b) are visual, mathematically accurate, representations of the SPB model using Fermi-Dirac statistics.

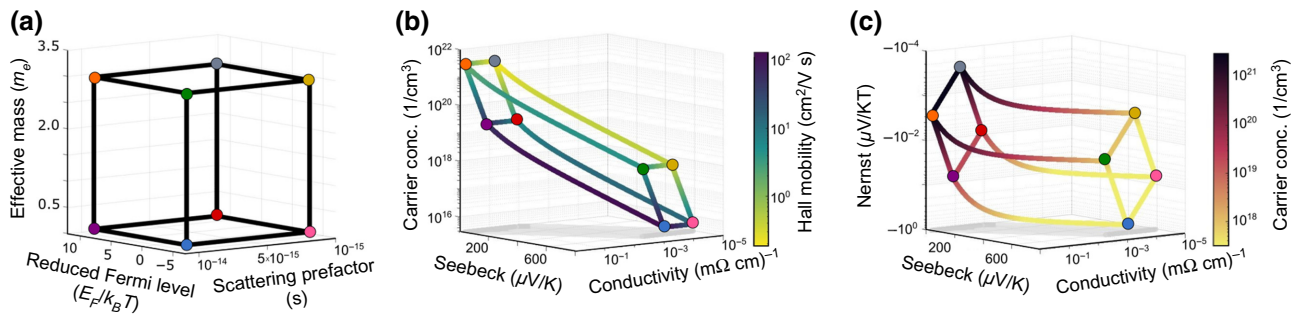


FIG. 2. (a) By defining a  $\mathbb{R}_3$  domain of material properties we transform this space using the single-parabolic band model (b) to the analogous  $\mathbb{R}_3$  space of transport coefficients assuming acoustic-phonon scattering with  $r = 0$ . The traditionally used Hall mobility has been calculated and heat mapped to this volume for clarity. (c) With the same assumption of  $r = 0$ , one can likewise use the method of four coefficients to transform these material properties to  $\mathbb{R}_4$ . Because of the difficulty of plotting a four-dimensional space, the volume for the method of four coefficients has been represented here in three dimensions with a fourth-dimension heat mapped to its transformation. For both volumes, the colored points serve as guides to the eye for orienting how the vectors in the domain transform through each analysis.

While the SPB model is a simple analysis approach to tackle thermoelectric transport, it does have its pitfalls. Imagine a case where the Fermi level and effective mass in the system are fixed but  $\tau_0$  and the scattering exponent could change. By changing  $r$ , you could detect increases in the Seebeck coefficient and conductivity. Without knowledge of scattering, this effect is often linked to changes in the effective mass [44,45] when it could be a scattering effect change. In doing so, the SPB model has the potential to pigeon-hole analyses based off its assumptions of fixed scattering mechanisms. We revisit such case examples in the following sections.

### III. THE METHOD OF FOUR COEFFICIENTS

The SPB model measures three coefficients to solve for three unknown material parameters. In order to eliminate the assumption of scattering source, a fourth transport coefficient needs to be introduced to solve a system of equations with four unknowns. This process, known colloquially as the method of four coefficients [28], utilizes a different galvanothermometric measurement: the Nernst coefficient ( $N$ ). This effect, a thermal analogue to the Hall effect, generates a transverse voltage ( $y$  direction) when an orthogonal temperature gradient ( $x$  direction) and magnetic field ( $z$  direction) are applied ( $|N| = E_y/B_z T_x$ ) [18,46]. Though often attributed with needing high mobility for a large Nernst signal, the magnitude of the Nernst coefficient depends on all four materials parameters ( $\eta$ ,  $m^*$ ,  $\tau_0$ , and  $r$ ):

$$N = \frac{k_B \tau_0}{c m^*} \frac{F_{r+1}(\eta)F_{2r+3/2}(\eta) - F_{2r+1/2}(\eta)F_{r+2}(\eta)}{[F_{r+1}(\eta)]^2}. \quad (11)$$

We see that the Nernst effect scales directly with mobility prefactors ( $\mu \propto \tau_0/m^*$ ), but is also a function of both the reduced Fermi level ( $\eta$ ) and scattering exponent ( $r$ ) [40]. As such, the introduction of the Nernst effect allows us to eliminate the assumption of the scattering exponent by combining the Nernst coefficient with the other three transport coefficients, as seen in Fig. 1(b).

This method yields a continuous range of scattering exponent values. As noted above, rational number scattering exponents emerge from various scattering types (i.e., acoustic-phonon scattering:  $r = 0$ ) [40]. As a result, an irrational exponent suggests the presence of scattering from multiple effects. Since the method of four coefficients does not fix the scattering to a particular mechanism, it gives us the ability to solve for this value.

While the SPB three-coefficient approach had a clear order of operations to solve for the material parameters, the method of four coefficients does not. The luxury of sequential processing is lost in the method of four coefficients and all material parameters ( $\eta$ ,  $m^*$ ,  $\tau_0$ , and  $r$ ) must be solved for simultaneously [Fig. 1(b)]. Similar to the SPB

model, the method of four coefficients assumes a single-parabolic band and, as such, this assumption should be tested via multiple samples at various carrier concentrations to ensure the application of these equations. Here we provide a road map to the intricacies of the method of four coefficients and how each transport coefficient is affected by the four underlying material parameters of interest.

#### A. Functional dependencies in the method of four coefficients

The thermoelectrics community has built an intuition for how the traditional thermoelectric effects change when we alter the Fermi level, but lacks intuition on how they change when scattering mechanisms change. We begin by walking through familiar trends in the Seebeck coefficient and carrier concentration to orient the reader.

In Fig. 3(a) we plot both the Seebeck coefficient and carrier concentration from Eqs. (6) and (8), respectively. We see that, as the Fermi level rises from the band gap to deep into the band, the magnitude of the carrier concentration increases and the Seebeck coefficient decreases as expected. The solid curve is generated assuming a fixed relaxation time, acoustic-phonon scattering ( $r = 0$ ), an effective mass, and an infinitely large band gap. The absolute value of the Seebeck coefficient is used to describe transport via electrons for clarity. Since we are no longer limited by restrictions of fixed scattering exponents, we can probe how these effects will change as a function of scattering.

The dashed curve in Fig. 3(a) highlights how impactful different scattering effects are on the Seebeck coefficient. If we have a material system that has a Fermi level right at the band edge ( $\eta = 0$ ) as is typical for optimized thermoelectric materials, the difference in the Seebeck coefficient between ionized impurity ( $r = 2$ ) and acoustic-phonon scattering ( $r = 0$ ) differs by almost a factor of 2. Unsurprisingly, the carrier concentration is unaffected by the influence of scattering, as one would expect, given Eq. (8) does not depend on  $r$ . In the same vein, one could expect differences to emerge for both the Hall coefficient [Eq. (7)] and conductivity [Eq. (5)] when the scattering exponent changes [see Figs. 4(d) and 4(b), respectively, of the Supplemental Material [41]].

In Fig. 3(b), the mobility is plotted as a function of various scattering exponents from Eq. (10). Again, we keep the same  $\tau_0$  and  $m^*$  fixed from before. Though we have fixed our mobility prefactors ( $\tau_0$  and  $m^*$ ), it can be seen that changing the scattering exponent alone can alter mobility significantly. Here we see the highest values of mobility for ionized impurity scattering and the lowest for acoustic-phonon scattering. As the Fermi level goes further into the band, thus increasing the carrier concentration, ionized impurity scattering increases while mobility for  $r = 0$  begins to decline.

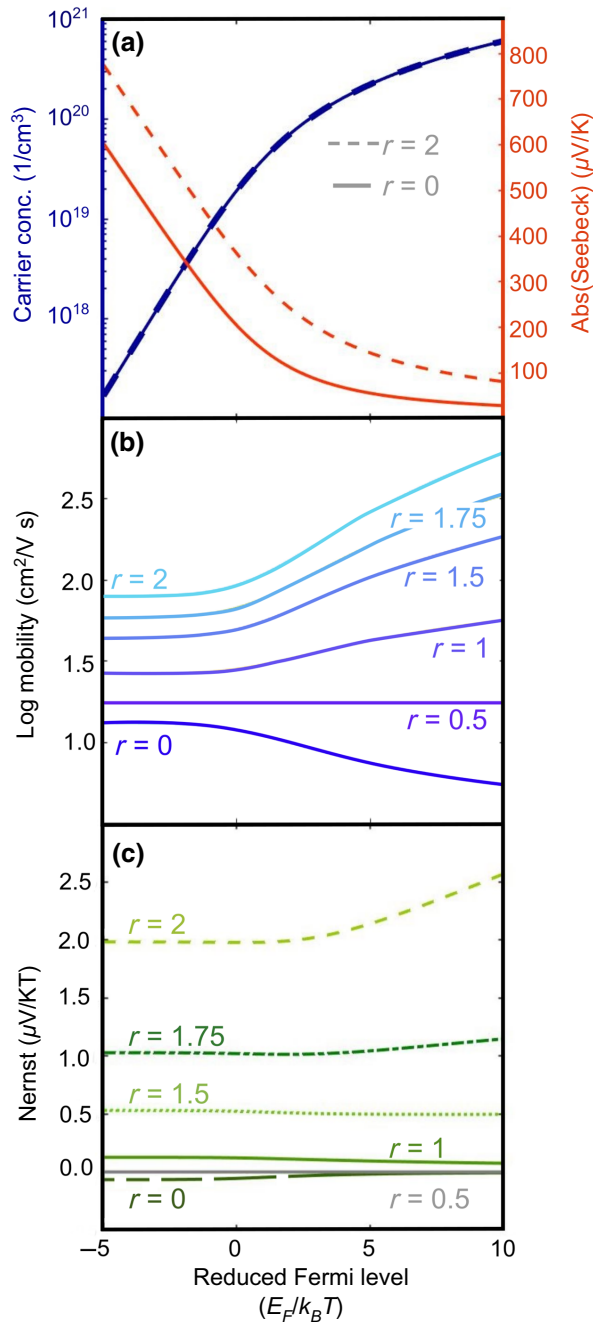


FIG. 3. Trends in measurable transport coefficients are calculated as a function of the reduced Fermi level ( $\eta$ ) and various scattering exponents ( $r$ ) (a)–(c). All graphs assume a single-parabolic band with transport occurring at a temperature of 300 K and assume a scattering time ( $\tau_0 = 1 \times 10^{-14}$  s) and an effective mass ( $m^* = 1m_e$ ). As the dominate scattering mechanism changes in the system, thus changing the value of the scattering exponent, we observe expected changes in the Seebeck effect and conductivity (a) and mobility (b). Here we see that the Nernst coefficient (c) does not heavily depend on Fermi level position but rather what scattering mechanism is dominate. Other material property trends and their effects on the Nernst coefficient can be seen in Figs. 1(c)–6(c) of the Supplemental Material [41].

For the Nernst coefficient, a consideration of Eq. (11) readily reveals the importance of large  $\tau_0$  and small  $m^*$  for a large signal. However, the impacts of  $\eta$  and  $r$  within the Fermi integrals are difficult to deduce by inspection. In Fig. 3(c), we calculate how the Nernst coefficient changes as a function of the Fermi level and various scattering mechanisms. Again, we keep  $\tau_0$  and  $m^*$  fixed to the same values. As one can see, for a single-parabolic band, the sign of the Nernst coefficient depends only on the scattering exponent,  $r$ . For  $r < 0.5$ , the Nernst coefficient is negative while all values greater than 0.5 yield a positive Nernst coefficient. A material system with higher values of  $r$ , such as is the case for ionized impurity scattering or polar optical phonon scattering, should yield the largest signals and thus make measurement viable. See Figs. 4(c)–6(c) of the Supplemental Material [41] for how the Nernst coefficient changes as a function of the effective mass and scattering time.

Since we assumed a scattering time and effective mass in Fig. 3, these are slices within the four-dimensional  $\mathbb{R}_4$  range of the method of four coefficients. We progressively expand this subspace to consider the interdependence of the transport coefficients to scattering parameter. First we consider the  $\mathbb{R}_3$  (three-dimensional) space of the method of four coefficients for an assumed  $r$ ; see Fig. 2(c).

Similar to the approach taken with the SPB model in the section above, we can utilize the four equations of the electronic transport coefficients and map out the expected  $\mathbb{R}_3$  space for realistic material parameters. We keep the same material parameters outlined in Fig. 2(a). For now, we hold  $r$  constant at  $r = 0$  for easier comparison between the two models. All the colored points in Fig. 2 serve as guides to the eye for the transformation process of each vector and, as a result, their subsequent dependencies on the transport coefficients can be examined.

Imagine a system that exists on the blue point in Fig. 2(a). The blue point has a high  $\tau_0$ , low  $m^*$ , and a Fermi level in the band gap. We saw from Eq. (11) that the Nernst coefficient scales with mobility (since mobility is proportional to  $\tau_0/m^*$ ). Indeed, we see that this high mobility point in blue has a large Nernst coefficient in Fig. 2(c). Now if we were to push the reduced Fermi level into the band but keep  $\tau_0$  and  $m^*$  fixed, we would be walking along the blue-to-purple point vector in Fig. 2(a). We can see how this vector is transformed by the method of four coefficients in Fig. 2(c). As we transverse the blue-to-purple vector in Fig. 2(c), we see a decrease in the magnitude of the Nernst coefficient (for  $r = 0$ ). This is self-consistent with the trends observed in Fig. 3(c) for acoustic-phonon scattering.

In Fig. 2 we held the scattering parameter constant for acoustic-phonon scattering at  $r = 0$ . In reality, the method of four coefficients curses us with an unknown scattering mechanism. In practice,  $r$  can be swept between  $0 < r < 2$

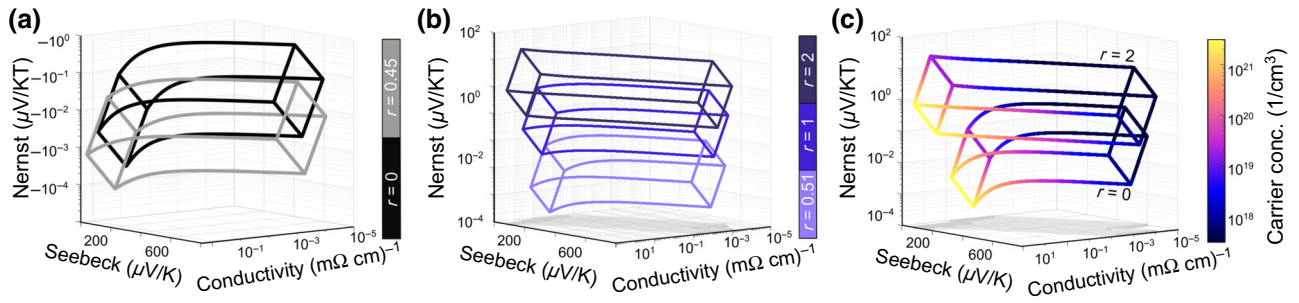


FIG. 4. The four-dimensional space of the method of four coefficients has been plotted in various  $\mathbb{R}_3$  sections using Fig. 2(a) as the input domain and Eqs. (5)–(11). For scattering exponents less than 0.5, the Nernst coefficient will be negative for a single-parabolic band (a). All values greater than 0.5 yield a positive Nernst coefficient (b). For energy-independent scattering ( $r = 0.5$ ), the Nernst coefficient goes to zero. To highlight the difference in magnitude between ionized impurity scattering ( $r = 2$ ) and acoustic-phonon scattering ( $r = 0$ ), the absolute value of the Nernst coefficient has been plotted in (c) for comparison. The two differ by roughly 2 orders of magnitude. The fourth dimension, the carrier concentration calculated from the Hall coefficient and the correct Hall factor, has been heat mapped for clarity.

to see how this space evolves as a function of the scattering parameter. As a result, this space is most accurately represented by a four-dimensional hypercube, a tesseract. Because of the challenges of plotting in a four-dimensional space, instead we investigate projections in  $\mathbb{R}_3$ . We can plot these transformation volumes for various values of  $r$ , as seen in Fig. 4. In Fig. 3(c), the sign of the Nernst coefficient switches upon crossing  $r = 0.5$ ; Fig. 4(a) presents the case for  $r < 0.5$  while Fig. 4(b) shows the regime where  $r > 0.5$ . To consider the difference in magnitude between these scenarios, the two datasets are overlaid in Fig. 4(c) with the fourth dimension (carrier concentration) plotted instead. Two separate plots are shown for the Nernst coefficient so that logarithmic axes can be used for both the negative and positive results. These two scattering mechanisms are highlighted as they are often the focus of bulk thermoelectrics materials near room temperature.

Unfortunately, the magnitude of the Nernst coefficient will yield small measurement signals for all scattering cases, as seen in Fig. 4. It is particularly noxious for the case of acoustic-phonon scattering since the signal is so close to zero. As such, highly accurate measurements will be needed to discern such a low Nernst coefficient. However, the differences in the sign of the Nernst coefficient between acoustic-phonon and ionized impurity scattering is a quick way to determine which mechanism is prominent in a system.

By adjusting the scattering parameter, we probe portions of this four-dimensional space. As can be seen in Fig. 4, there exists no torsion or twists to these volumes, leading us to infer that this is a unique transformation. Indeed, upon inspection, no two calculated points are the same. Every point across the material property domain space we highlighted has a unique solution of transport coefficients. As such, we infer by inspection that the method of four

coefficients is a bijective transformation and a mathematically viable technique for determining underlying transport phenomena.

Having established the method of four-coefficient analysis and the associated  $\mathbb{R}_4 \rightarrow \mathbb{R}_4$  transformation, we briefly investigate the uncertainty that remains in the three-coefficient SPB analysis approach. As a first case example, we consider our prior SPB analysis of  $\text{Yb}_{14}\text{Mn}_{0.8}\text{Al}_{0.2}\text{Sb}_{11}$  from Ref. [47]. This sample exhibited the following properties: a Seebeck coefficient of  $55 \mu\text{V/K}$ ; a carrier concentration of  $1.2 \times 10^{21} \text{ cm}^{-3}$ ; and a resistivity of  $2 \text{ m}\Omega \text{ cm}$ . By applying the SPB model to this point, these transport coefficients yield the material parameters given by the red circle labeled  $\text{Yb}_{14}\text{Mn}_{0.8}\text{Al}_{0.2}\text{Sb}_{11}$  in Fig. 5. However, since no information about the Nernst coefficient is reported, we can hypothesize that this sample could display any reasonable Nernst values ( $-0.005 \mu\text{V/KT} \leq N \leq 0.0075 \mu\text{V/KT}$ ), moving the experimental data from a point in  $\mathbb{R}_3$  to a line in  $\mathbb{R}_4$ .

We can then transform this  $\mathbb{R}_4$  line using Eqs. (5)–(11) to determine how this space would be analyzed under the method of four coefficients (Fig. 5,  $\text{Yb}_{14}\text{Mn}_{0.8}\text{Al}_{0.2}\text{Sb}_{11}$ ). Without information about the Nernst coefficient, this  $\mathbb{R}_3$  subspace could span from the red circle all the way to the end of the line (yellow). The three traditional transport coefficients could then yield the following ranges:  $\mathbf{5.1} \leq \eta(E_F/k_B T) \leq 15.0$ ;  $1.02 \leq m^*(m_e) \leq \mathbf{3.01}$ ;  $2.7 \times 10^{-17} \leq \tau_0(s) \leq \mathbf{1.1} \times 10^{-14}$ . Here, the bold values correspond to  $r = 0$  and the nonbold values correspond to  $r = 2$ .

We see that the same pattern holds for other material systems analyzed under the single-parabolic band approach such as  $\text{EuZn}_2\text{Sb}_2$ ,  $\text{Tl}_{0.02}\text{Pb}_{0.98}\text{Te}$ , and  $\text{Ba}_8\text{Ga}_{15.75}\text{Ge}_{30.25}$  [14,16,48]. In all these cases, the assumption that  $r = 0$  results in a solution on the extreme of the possible range of material parameters. Despite these concerns about the use

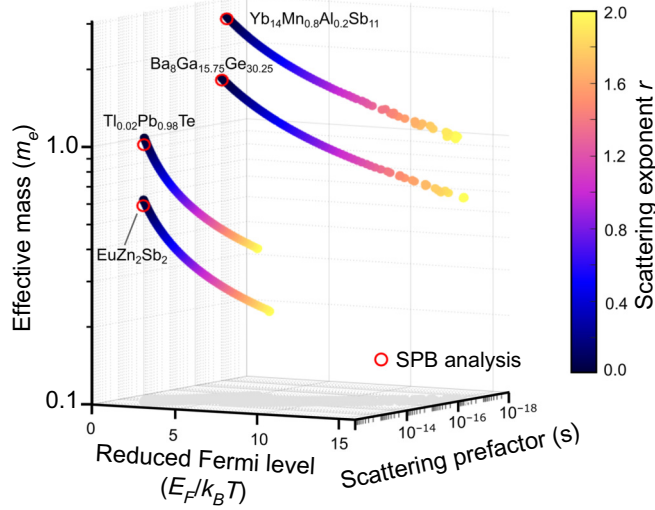


FIG. 5. Here we take four material systems from the literature [14,16,47,48] that have applied the SPB model and calculate the method of four coefficients for all values of the Nernst coefficient. This allows us to solve the range of material parameters that would be correct solutions for the SPB approach. Typically, the SPB approach assigns  $r = 0$  for acoustic-phonon scattering, but for these curves, it spans from  $r = 0$  to 2. The red points correspond to the properties as per calculated by the SPB model. The slight offset from the calculated data can be attributed to not using the scattering-exponent-dependent Hall factor (since SPB assumes that  $a_r = 1$ ).

of the SPB model and the associated assumption of scattering, there is a practical utility to calculating an “effective” effective mass as Nernst measurements could ultimately be challenging to obtain for compounds with low mobility. However, this exercise shows that the scattering exponent used in the analysis could lead to a variation in the effective mass by half an order of magnitude, a variation in the reduced Fermi level by about 10 (e.g., 260 meV at room temperature), and a scattering prefactor varying by 3 orders of magnitude.

#### IV. ERROR PROPAGATION OF THE FOUR-COEFFICIENT ANALYSIS

Though solving for a range of transport coefficients is insightful to observe trends, an experimentalist is often faced with the problem in reverse. Sadly, the transformations from  $\mathbb{R}_4$  of the transport coefficients to  $\mathbb{R}_4$  of the material parameters is much more difficult. Instead of having the luxury of piping variables through an analytic solution, one must deconvolute the Fermi integrals and untangle the material parameters from the integrands. To do so, numerical integration and a backsolving search process must be performed on the set of equations (8)–(11) simultaneously. In this section we determine the material properties by their transport coefficient using the full

Fermi-Dirac statistics. This will allow us to prescribe experimental error to the transport coefficients and probe how the error propagates through this analysis technique.

#### A. Methods of numerical integration

It is common to use Fermi integral look-up tables to determine the value of the Fermi integrals; however, this assumes one scattering exponent. Since we are searching a continuous range of  $r$ , we calculate the Fermi integrals using the  $n$ -point Gauss-Laguerre quadrature method. This technique allows us to numerically integrate our transport equations: Eqs. (5)–(11). This process evaluates an integral by calculating the sum of the product of the weights ( $w_i$ ) multiplied by the integrand’s  $f(x)$  at a specific node ( $x_i$ ):

$$\int_0^{\infty} f(x)e^{-x} dx = \sum_{i=1}^n w_i f(x_i). \quad (12)$$

The nodes  $x_i$  are the roots of the  $n$ th-order Laguerre polynomial and the weights are computed by solving the following for each integer  $k$  from 0 to  $n - 1$ :

$$\int_0^{\infty} x^k e^{-x} dx = \sum_{i=1}^n w_i f(x_i). \quad (13)$$

To compute the Fermi Integrals, we used the following  $f(x)$  to cancel out the  $e^{-x}$  term built into the quadrature definition:

$$f_k(x, \eta) = \frac{e^{x-\eta}}{(1 + e^{x-\eta})^2} x^k e^x. \quad (14)$$

The Gauss-Laguerre quadrature computed integral of  $[-\partial f_0(x, \eta = 0)/\partial x]$  with  $n = 100$  matched the computed value of the built-in integrate command in MATLAB<sup>®</sup> to machine precision. As such, weights and nodes are calculated to  $n = 100$  for all calculations in this paper. We adapted open-source Gauss-Laguerre quadrature code to fit the analysis [49].

To begin the backsolving process, we define a range of guesses for each of the material parameters:  $r \in [0, 2]$ ,  $\eta \in [-5, 10]$ ,  $m^* \in [0.1, 5]$  ( $m_e$ ),  $\tau_0 \in [10^{-14}, 10^{-15}]$  (s). These values are determined by forward-solving Eqs. (5)–(11) for various transport coefficients to ensure that our starting ranges encompass our resulting domain. Each range is then divided into equally spaced points with a grid spacing of thirty. Combinations of this grid are then used to calculate a range of transport coefficients. A cost function [Eq. (8) within the Supplemental Material [41]] is then applied to each of the calculated values. This function compares the true transport coefficient values to each of the combinations calculated from our starting ranges. The point with minimum cost is then specified.

To ensure that we are not constraining our system to the initial starting ranges of the material parameters, if the point with minimum cost is on the edge of the starting hypercube, we shift our ranges with the point of minimum cost at the center of the ranges. Then the grid is recalculated as before. This process is performed until the point of minimum cost is no longer on an edge case of the hypercube.

Once this is verified, the search window is centered around the point with minimum cost and we reduce the range sizes by 1/5 to calculate a finer grid search. This finer mesh goes through the same process as before, stepping down continuously until the material parameter ranges ( $\{\Delta r, \Delta \eta, \Delta m^*/m_e, \Delta \tau_0 \times 10^{15} \text{ s}^{-1}\}$ ) can be determined within a tolerance of 0.001. The system then outputs a coordinate in  $\mathbb{R}_4$  of material parameters ( $r, \eta, m^*, \tau_0$ ) for the provided transport coefficients ( $\alpha, \sigma, R_H, N$ ). All calculations are executed in MATLAB in Gaussian units and converted to SI units post integration.

Sequential integration of Eqs. (5)–(11) is implemented as all transport equations are needed in determining convergence to a unique point in the material parameter space. To verify our results and ensure that we are not in any local minima, we compare all numerically integrated points to the analytic forward-solving approach (as used in the sections above). Indeed, all numerically integrated points are within machine precision to their analytic counterparts. Therefore, all sets of transport coefficients can be used to solve for their unique material parameters (within our set of assumptions) through their full Fermi-Dirac equations by the method of four coefficients. This gives us the flexibility to forward or backward solve this set of equations.

### B. Error in transport measurements

Assessing the error when transforming from material parameters to transport coefficients can be addressed analytically. Practically, however, the backsolving process of transforming experimental transport coefficients to material parameters precludes a simple error analysis. In the

following we intentionally perturb the experimental transport coefficients with combinations of small errors. This effort relies on the unique transformation between these two spaces.

As a case study, we prescribe the following error bars to each of the transport coefficients:  $\pm 2\%$  conductivity,  $\pm 5\%$  Seebeck,  $\pm 5\%$  Hall,  $\pm 10\%$  Nernst plus an additional  $\pm 0.05 \mu\text{V}/\text{KT}$ . A small error has been prescribed to conductivity, but depending on which geometry is used during measurement (van der Pauw or Hall bar set up) the error may be larger. As a result, an analysis with  $\pm 10\%$  conductivity error may be found in the Supplemental Material [41]. Likewise, the addition of spot-welded thermocouples can decrease the error in Seebeck measurements leading to errors as low as one percent. In this case, we focus on a larger Seebeck error likely associated with pressure-based contacts; however, the supplemental error analysis in the Supplemental Material [41] uses  $\pm 3\%$  for the Seebeck coefficient.

A large Nernst error has been applied since Nernst measurements are not commonly utilized, and the expected coefficient would yield low signals, as evident by Fig. 4. While Nernst measurements can be more accurate, proper instrumentation design is needed to achieve this goal. In this case study, this large error should serve as a cautionary tale when designing Nernst apparatuses. For example, proper thermal gradient assessment and thermal contact resistances are critical to the success of this measurement. Failure to properly account for off-set contacts can lead to the breakdown of the isothermal approximation along the  $y$  axis and extraneous transport (such as magneto-Seebeck) can be measured instead. Since there are several research groups that perform Nernst measurements regularly, the supplemental error analysis case study (see the Supplemental Material [41]) includes analysis with decreased Nernst error.

For the large prescribed Nernst error, both a relative and static error is added. In the simplest form, the error propagation in the Nernst measurement scales as

$$\sigma_N = N \sqrt{\left(\frac{\sigma_{l_x}}{l_x}\right)^2 + \left(\frac{\sigma_{l_y}}{l_y}\right)^2 + \left(\frac{\sigma_{B_z}}{B_z}\right)^2 + \left(\frac{\sigma_{\Delta V}}{\Delta V}\right)^2 + \left(\frac{\sigma_{\Delta T}}{\Delta T}\right)^2}, \quad (15)$$

where  $l_x$  and  $l_y$  are lengths,  $B_z$  is the magnetic field in the  $z$  direction,  $\Delta V$  is the voltage,  $\Delta T$  is the temperature, and  $N$  is the Nernst coefficient. We highlight the  $N$  outside of the square root; the error will scale with the magnitude of the component errors and the overall signal. In brief, the primary conclusions of this section of the article are not

significantly altered by reducing the error of the Nernst measurement (see the Supplemental Material [41]).

The results of this case study of error assessment are shown in Fig. 6. To begin, we choose a point in our domain as a starting seed value ( $\{r = 1, \tau_0 = 5 \times 10^{-15} \text{ (s)}, m^* = 1m_e, \eta = 1\}$ ). This point is then used

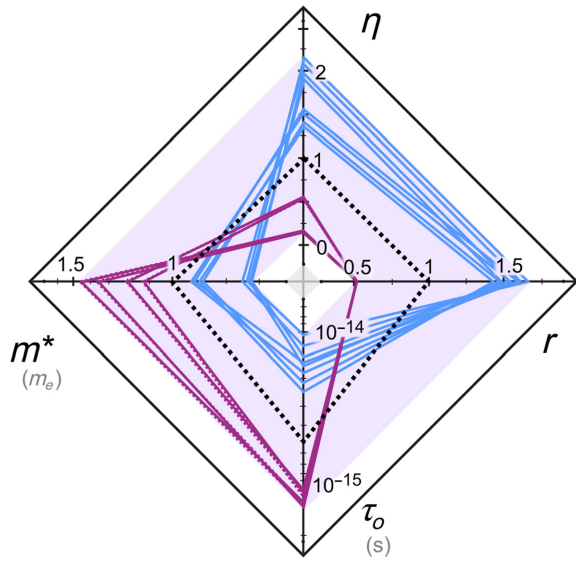


FIG. 6. To investigate how experimental error propagates through the method of four coefficients, we begin with a starting seed value of material parameters (black dashed line) and analytically solve for the transport coefficients:  $\{\alpha = -283 \text{ } (\mu\text{V/K}), \sigma = 0.04 \text{ } (\text{m}\Omega \text{ cm})^{-1}, N = 0.06 \text{ } (\mu\text{V/KT}), n = 1.9 \times 10^{19} \text{ } (1/\text{cm}^3)\}$ . A systematic error is then prescribed to each of the transport coefficients and the 16 combinations of error are plotted here. This allows us to bound the region of error by the purple shaded overlay. Regions of high Nernst and low Nernst errors have been separated (blue and purple, respectively) and it is clear that this causes a larger range in error as these two regions are distinct.

to calculate the expected experimental transport coefficients via the analytic Eqs. (5)–(11). In the case example considered here, this yields  $\{\alpha = -283 \text{ } (\mu\text{V/K}), \sigma = 0.04 \text{ } (\text{m}\Omega \text{ cm})^{-1}, N = 0.06 \text{ } (\mu\text{V/KT}), n = 1.9 \times 10^{19} \text{ } (e^-/\text{cm}^3)\}$ . The prescribed errors are then assigned to the calculated coefficients. Since there are four transport coefficients, each with their own minimum and maximum errors, we calculate each combination of error leading to a set of sixteen points ( $2^4$ ) in this four-dimensional space. These sixteen points coarsely describe the region of potential error surrounding a set of experimental coefficients. All sixteen points and the starting coefficient value are then piped through the numerical integration process to calculate the expected value of the material properties. This can be seen by the purple shaded region in Fig. 6. The individual combinations have been separated by high and low Nernst errors using blue and purple lines, respectively. For this case example, the assigned error in coefficients yield the following ranges in material properties:  $0.51 < r < 1.67$ ,  $0.17 < \eta < 2.19$ ,  $0.72 < m^* < 2.19$ ,  $1.03 \times 10^{-15} < \tau_0 < 1.33 \times 10^{-14}$ .

The  $\mathbb{R}_4$  tesseract of material properties is found to have widely varying error propagation when applying the method of four coefficients. To explore this range, Fig. 7

traverses this tesseract using the same notation as found in Fig. 6 [these same results are replicated in Figs. 7(a) and 7(b) as a legend]. Note that the axes have been expanded in Fig. 7(b) and the figure has been simplified to show only the “true” value and the range of error, denoted by the purple shaded region. The Nernst axis is on a cube root as it spans both positive and negative values. The solid purple lines of Figs. 7(a) and 7(b) are the direct transform of the other.

Figures 7(c)–7(f) show a selection of points across the tesseract to see trends in the error. Here we have chosen seed values near all the extrema of  $\mathbb{R}_3$  in Figure 2(a) and  $r = 0, 2$ . The two rows describe the transport coefficients and material parameters, respectively, while the two columns involve systems with low and high  $\tau_0$ . Within each panel, the cube is decorated with eight diamonds, the legends for which are shown in panels (a) and (b). The coordinate system within each cube is shown by the axes in the center. In the following we use a simple indexing [shown explicitly in Fig. 7(c)] where the origin is  $(0, 0, 0)$  and corresponds to low effective mass, small  $r$ , and a low reduced Fermi level.

Figure 7 reveals that regions of largest error are associated with low  $\tau_0$  and large  $m^*$  [e.g., corner  $(0, 1, 1)$  of panel (d)]. Conversely, the error decreases for large  $\tau_0$  and low  $m^*$  [e.g., corner  $(0, 0, 1)$  of panel (f)]. This trend is primarily due to the dependence of the Nernst coefficient magnitude on these two parameters [Eq. (11)]. Similar trends can be seen for the  $(0, 1, 0)$  panel (c) and  $(0, 0, 0)$  panel (f) pair and related pairings.

The reduced Fermi level and scattering exponent also play significant roles in determining the error in the method of four coefficients. As seen in Fig. 3(c), for  $r < 1$ , the magnitude of the Nernst coefficient is quite small. The impact of such a weak Nernst signal can be generally seen by direct comparison of the left and right sets of points, i.e.,  $(h, k, 0)$  versus  $(h, k, 1)$ . In all cases, the increase in  $r$  reduces the error. This issue is further compounded at high  $\eta$  for samples with small  $r$ . Figure 3(c) highlights that these compounds exhibit exceptionally weak Nernst signals, leading to significant error in data analysis. For example, point  $(0, 0, 1)$  in panel (d) has significant uncertainty due to the small value of  $N$  at large  $\eta$  for  $r = 0$ . Transitioning to  $r = 2$  eliminates this null value for  $N$  and dramatically decreases the error. For comparison, the change in  $r$  created by transitioning from panel (d)  $(0, 0, 0)$  to  $(1, 0, 0)$  shows minimal error in both samples due to the strong  $N$  signal for  $r = 2$ .

## V. CONCLUSIONS

Understanding charge-carrier dynamics in semiconductors is inherently difficult due to the ensemble averaging in common measurements. Further compounding the problem is that semiconductors possess a rich array of

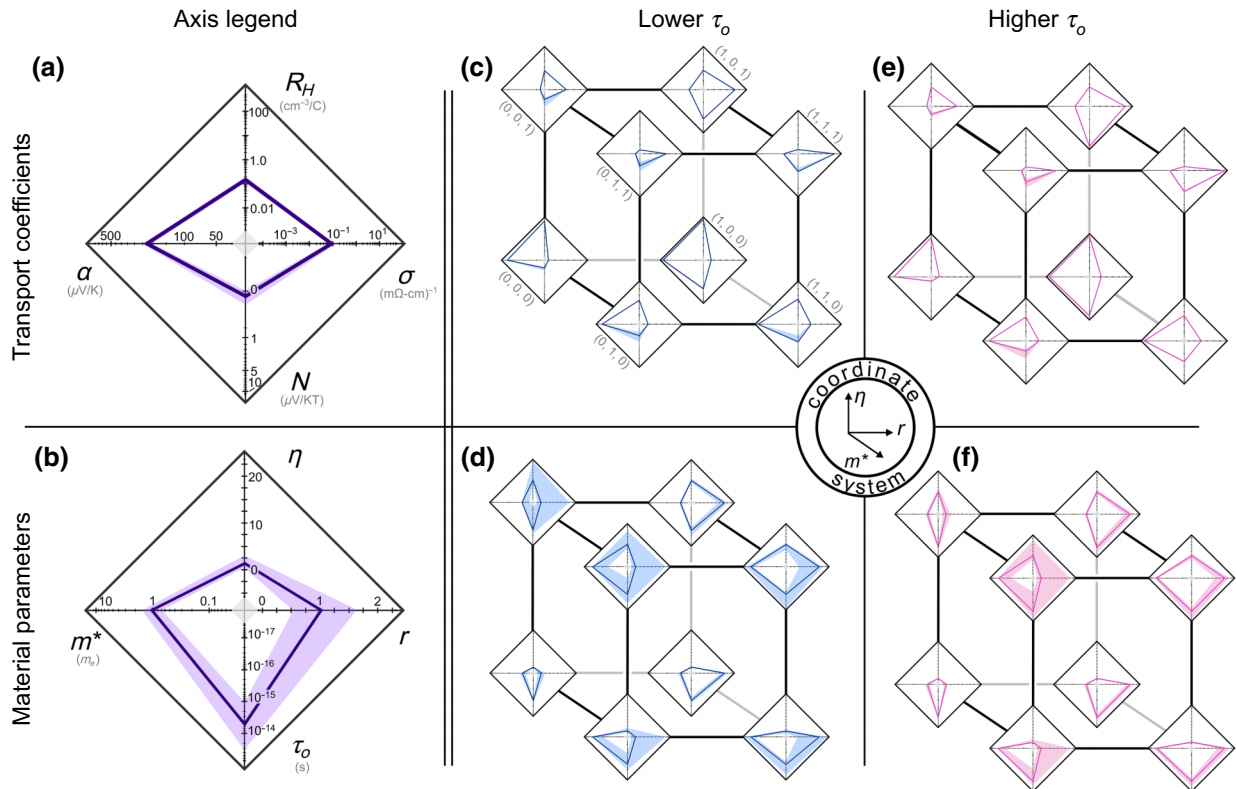


FIG. 7. Experimental error is assigned to transport coefficients to observe how the method of four coefficients propagates error. Without error in the measurables [(a)—dark purple solid line], the method of four coefficients can solve for a unique solution for the set of scattering exponent, scattering time, effective mass, and reduced Fermi level. Once the experimental error is assigned to the transport coefficients [(a)—purple shaded region], the error in the material parameters can be numerically assessed [(b)—purple shaded region]. The purple radar plots serve as the axis legends for all the radar plots in the subsequent panels. We calculate a set of experimental data points near all the extrema in Fig. 2(a) and for  $0 < r < 2$ . A standard experimental error is then applied to all coefficients and the error in material parameters is calculated. The radar plots are overlaid onto their initial seed values with the coordinate system labeled. Seed values with low and high  $\tau_0$  have been plotted separated for clarity.

scattering sources (various defects, spectrum of phonons, etc.) that contribute to charge-carrier scattering. As such, there is a persistent need to more accurately model the energy dependence of charge-carrier scattering if we are to understand the connection between chemical structure and transport physics. Nernst coefficient measurements have sporadically been conducted over the last century and a half and have occasionally been incorporated into a multicomponent analytic approach known as the method of four coefficients. In this work, we explore the interdependencies between the four material parameters and their four associated transport coefficients. Within the parabolic band assumption, the  $\mathbb{R}_4$  to  $\mathbb{R}_4$  transformation is found to be mathematically unique. Our exploration of the transformation space provides guidance to experimentalists on the expected magnitudes of the pertinent transport coefficients as a function of material properties. Case examples of materials previously analyzed by the single-parabolic band model are reanalyzed to determine the possible solution space that could have been obtained with Nernst measurements. We find that the assumption of scattering

coefficient traps analysis to a small subset of the potentially correct solution space. Having shown the potential for the method of four coefficients to successfully distinguish between changes in  $m^*$ ,  $\eta$ ,  $\tau_0$ , and  $r$ , we consider the impact of experimental error on such an analysis. The error propagation revealed that areas with low mobility yield large error due to the low value of  $N$  and that high  $\eta$  and small  $r$  can be challenging as well. While the method of four coefficients does not overcome the challenge of ensemble averaging of charge-carrier dynamics, we ultimately conclude that the inclusion of Nernst measurements and the associated method of four coefficients provide critical insight into charge-carrier scattering.

## ACKNOWLEDGMENTS

This work was performed at the California Institute of Technology/Jet Propulsion Laboratory under contract with the National Aeronautics and Space Administration. This work is supported by the NASA Science Mission

Directorate's Radioisotope Power Systems Thermoelectric Technology Development Project under Grants No. NNX16AT18H and No. 80NSSC19K1290. We also acknowledge support from the National Science Foundation (NSF) under Grants No. 1555340 and No. 1950924.

- [1] M. Dresselhaus, G. Chen, M. Tang, R. Yang, H. Lee, D. Wang, Z. Ren, J.-P. Fleurial, and P. Gogna, New directions for low-dimensional thermoelectric materials, *Adv. Mater.* **19**, 1043 (2007).
- [2] G. J. Snyder and E. S. Toberer, Complex thermoelectric materials, *Nat. Mater.* **7**, 105 (2008).
- [3] M. Lundstrom, in *Fundamentals of Carrier Transport*, Vol. 1 (Cambridge University Press, Cambridge, UK, 1990), 2nd ed.
- [4] M. Wood, U. Aydemir, S. Ohno, and G. J. Snyder, Observation of valence band crossing: The thermoelectric properties of  $\text{CaZn}_2\text{Sb}_2$ - $\text{CaMg}_2\text{Sb}_2$  solid solution, *J. Mater. Chem. A* **6**, 9437 (2018).
- [5] K. Behnia and H. Aubin, Nernst effect in metals and superconductors: A review of concepts and experiments, *Rep. Prog. Phys.* **79**, 1 (2016).
- [6] S. Zukotynski and J. Kolodziejczak, On the determination of the non-parabolicity of energy bands, *Phys. Status Solidi* **19**, K51 (1967).
- [7] D. L. Young, J. F. Geisz, and T. J. Coutts, Nitrogen-induced decrease of the electron effective mass in  $\text{GaAs}_{1-x}\text{N}_x$  measured by thermomagnetic transport phenomena, *Appl. Phys. Lett.* **82**, 1236 (2003).
- [8] J. P. Heremans, C. M. Thrush, and D. T. Morelli, Thermopower enhancement in lead telluride nanostructures, *Phys. Rev. B* **70**, 1 (2004).
- [9] S. A. Nemov, V. A. Proshin, G. L. Tarantasov, R. V. Parafen, D. V. Shamshur, and A. V. Chernyaev, Transverse Nernst-Ettingshausen effect, resonant scattering, and superconductivity in  $\text{SnTe}$ : In, *Semicond. Dielectr.* **51**, 491 (2009).
- [10] J. P. Heremans, W. Bartłomiej, and A. M. Chamoire, Resonant levels in bulk thermoelectric semiconductors, *Energy Environ. Sci.* **5**, 5510 (2012).
- [11] D. J. E. Demars, J. Basinski, and J. C. Woolley, Nernst-Ettingshausen effects and electron scattering in  $\text{GaSb}$ , *J. Phys. C: Solid State Phys.* **7**, 1504 (1974).
- [12] G. J. Snyder and A. May, in *Materials, Preparation, and Characterization in Thermoelectrics*, edited by D. M. Rowe (CRC Press, Boca Raton, FL, 2012), 1st ed., chapter 11, p. 11-1.
- [13] H. J. Goldsmid, *Introduction to Thermoelectricity* (Springer, Berlin, Germany, 2010), 2nd ed.
- [14] A. F. May, E. S. Toberer, A. Saramat, and G. J. Snyder, Characterization and analysis of thermoelectric transport in  $n$ -type  $\text{Ba}_8\text{Ga}_{16-x}\text{Ge}_{30+x}$ , *Phys. Rev. B* **80**, 125205 (2009).
- [15] H.-S. Kim, Z. M. Gibbs, Y. Tang, H. Wang, and G. J. Snyder, Characterization of Lorenz number with Seebeck coefficient measurement, *APL Mater.* **3**, 041506 (2015).
- [16] J. P. Heremans, V. Jovovic, E. S. Toberer, A. Saramat, K. Kurosaki, A. Charoenphakdee, S. Yamanaka, and G. J. Snyder, Enhancement of thermoelectric efficiency in  $\text{PbTe}$  by distortion of the electronic density of states, *Science* **321**, 554 (2008).
- [17] M. K. Zhitinskaya, V. I. Kaidanov, and I. A. Chernik, Non-parabolicity of the conduction band of lead telluride, *Soviet Phys.-Solid State* **8**, 246 (1966).
- [18] D. M. Rowe, ed., *Thermoelectrics Handbook: Macro to Nano* (CRC Press, Boca Raton, FL, 2006), 1st ed.
- [19] I. M. Tsidil'kovskii, in *Thermomagnetic Effects in Semiconductors*, edited by H. Goldsmid (Academic Press Inc., New York, NY, 1962), 1st ed.
- [20] E. H. Putley, ed., in *The Hall Effect and Related Phenomena* (Butterworth & Co. Publishers, Washington D.C., 1960), 1st ed.
- [21] E. H. Hall, The four transverse effects and their relations in certain metals, *PNAS* **11**, 416 (1925).
- [22] E. H. Sondheimer, The theory of the galvanomagnetic and thermomagnetic effects in metals, *Proc. R. Soc. Lond. A* **193**, 484 (1948).
- [23] T. C. Harman, Galvano-thermomagnetic effects in semiconductors and semimetals—IV. Mercury selenide, *J. Phys. Chem. Solids* **25**, 931 (1964).
- [24] E. H. Putley, Thermoelectric and galvanomagnetic effects in lead selenide and telluride, *Proc. Phys. Soc. Section B Thermoelectr.* **68**, 35 (1955).
- [25] R. Mansfield and W. Williams, The electrical properties of bismuth telluride, *Proc. Phys. Soc.* **52**, 733 (1958).
- [26] H. J. Goldsmid, N. Savvides, C. Uher, The Nernst effect in  $\text{Cd}_3\text{As}_2$ - $\text{NiAs}$ , *J. Phys. D* **5**, 1352 (1972).
- [27] T. C. Hartman and J. M. Honig, Galvano-thermomagnetic effects in degenerate semiconductors and semimetals with non-parabolic band shapes: II. General theory, *J. Phys. Chem. Solids* **23**, 913 (1962).
- [28] C. M. Jaworski and J. P. Heremans, Thermoelectric transport properties of the  $n$ -type impurity Al in  $\text{PbTe}$ , *Phys. Rev. B* **85**, 1 (2012).
- [29] D. L. Young, T. J. Coutts, and V. I. Kaydanov, Density-of-states effective mass and scattering parameter measurements by transport phenomena in thin films, *Rev. Sci. Instrum.* **71**, 462 (2000).
- [30] V. Jovovic, S. J. Thiagarajan, J. P. Heremans, T. Komisarova, D. Khokhlov, and A. Nicorici, Low temperature thermal, thermoelectric, and thermomagnetic transport in indium rich alloys, *J. Appl. Phys.* **103**, 53710 (2008).
- [31] J. P. Heremans, C. M. Thrush, and D. T. Morelli, Thermopower enhancement in  $\text{PbTe}$  with Pb precipitates, *J. Appl. Phys.* **98**, 1 (2005).
- [32] T. J. Coutts, D. L. Young, X. Li, W. P. Mulligan, and X. Wu, Search for improved transparent conducting oxides: A fundamental investigation of  $\text{CdO}$ ,  $\text{Cd}_2\text{SnO}_4$ , and  $\text{Zn}_2\text{SnO}_4$ , *J. Vac. Sci. Technol., A* **18**, 2646 (2000).
- [33] D. L. Young, T. J. Coutts, V. I. Kaydanov, A. S. Gilmore, and W. P. Mulligan, Direct measurement of density-of-states effective mass and scattering parameter in transparent conducting oxides using second-order transport phenomena, *J. Vac. Sci. Technol. A* **18**, 2978 (2000).
- [34] N. H. Protik and B. Kozinsky, Electron-phonon drag enhancement of transport properties from a fully coupled

- ab initio Boltzmann formalism, *Phys. Rev. B* **102**, 245202 (2020).
- [35] T.-H. Liu, J. Zhou, B. Liao, D. J. Singh, and G. Chen, First-principles mode-by-mode analysis for electron-phonon scattering channels and mean free path spectra in GaAs, *Phys. Rev. B* **95**, 75206 (2017).
- [36] J.-J. Zhou and M. Bernardi, Ab initio electron mobility and polar phonon scattering in GaAs, *Rapid Commun. Phys. Rev. B* **94**, 201201 (2016).
- [37] B. Liao, J. Zhou, B. Qiu, M. S. Dresselhaus, and G. Chen, Ab initio study of electron-phonon interaction in phosphorene, *Phys. Rev. B* **91**, 235419 (2015).
- [38] Q. Song, T. H. Liu, J. Zhou, Z. Ding, and G. Chen, Ab initio study of electron mean free paths and thermoelectric properties of lead telluride, *Mater. Today Phys.* **2**, 69 (2017).
- [39] S. Bang, J. Kim, D. Wee, G. Samsonidze, and B. Kozinsky, Estimation of electron-phonon coupling via moving least squares averaging: A method for fast-screening potential thermoelectric materials, *Mater. Today Phys.* **6**, 22 (2018).
- [40] B. M. Askerov, *Electron Transport Phenomena in Semiconductors* (World Scientific Publishing Co., Singapore, 1994), 1st ed.
- [41] See Supplemental Material at <http://link.aps.org/supplemental/10.1103/PhysRevApplied.16.024004> for nomenclature definitions, unit conversions, an overview of transport coefficients with various graphs depicting functional dependencies, and a separate case study for error propagation.
- [42] M. Lundstrom, in *Near Equilibrium Transport: Fundamentals and Applications*, Vol. 2 (World Scientific Co., Singapore, 2013), 1st ed.
- [43] K. A. Borup, J. de Boor, H. Wang, F. Drymiotis, F. Gascoin, X. Shi, L. Chen, M. I. Fedorov, E. Müller, B. B. Iversen, and G. J. Snyder, Measuring thermoelectric transport properties of materials, *Energy Environ. Sci.* **8**, 423 (2015).
- [44] Y. Pei, H. Wang, and G. J. Snyder, Band engineering of thermoelectric materials, *Adv. Mater.* **24**, 6125 (2012).
- [45] T.-R. Wei, H. Wang, Z. M. Gibbs, C.-F. Wu, G. J. Snyder, and J.-F. Li, Thermoelectric properties of Sn-doped *p*-type  $\text{Cu}_3\text{SbSe}_4$ : A compound with large effective mass and small band gap, *J. Mater. Chem. A* **2**, 13527 (2014).
- [46] E. H. Butler Jr. and E. M. Pugh, Galvano- and thermomagnetic phenomena in iron and nickel, *Phys. Rev.* **57**, 916 (1940).
- [47] E. S. Toberer, C. A. Cox, S. R. Brown, T. Ikeda, A. F. May, S. M. Kauzlarich, and G. J. Snyder, Traversing the metal-insulator transition in a Zintl phase: Rational enhancement of thermoelectric efficiency in  $\text{Yb}_{14}\text{Mn}_{1-x}\text{Al}_x\text{Sb}_{11}$ , *Adv. Funct. Mater.* **18**, 2795 (2008).
- [48] E. S. Toberer, A. F. May, B. C. Melot, E. Flage-Larsen, and G. J. Snyder, Electronic structure and transport in thermoelectric compounds  $A\text{Zn}_2\text{Sb}_2$  ( $A = \text{Sr}, \text{Ca}, \text{Yb}, \text{Eu}$ ), *Dalton Trans.* **39**, 1046 (2010).
- [49] G. V. Damme, Legendre laguerre and hermite—gauss quadrature (2020), accessed Oct. 10, 2020.